Composites & nanocomposites

Vacuum-dried, low-density and robust hydrophobic bridged silsesquioxane aerogels for oil–water separation

Peijian Zhao[1], Linlin Wang[1,3], Lefu Xie[3], Lei Li[1,*], and Shengyu Feng[1,2,*]

[1] Key Laboratory of Special Functional Aggregated Materials (Shandong University), Ministry of Education, School of Chemistry and Chemical Engineering, Shandong University, Jinan 250100, People's Republic of China

[2] Key Laboratory of Colloid and Interface Chemistry (Shandong University), Ministry of Education, School of Chemistry and Chemical Engineering, Shandong University, Jinan 250100, People's Republic of China

[3] Weihai New Era Chemical Co., Ltd, Weihai 264205, People's Republic of China

ABSTRACT

Silica aerogels are attractive materials with many fascinating properties, however, their poor mechanical properties and the laborious drying methods strongly restrict their practical applications. Here, we reported the preparation of novel salicylaldimine-bridged silica aerogels. The 5,5'-methylene-bis-salicylaldimine bridging groups were efficiently introduced into aerogels via a facile ambient Schiff-base reaction. The obtained aerogels were constructed of large-sized colloidal particles (average diameter = 1 μm) and had a macroporous structure, which allows them to be prepared directly through a facile vacuum drying method. These aerogels exhibit high porosity (> 90%), ultra-low density (0.058 g cm^{-3}), high compression resistance (> 80% strain), good thermal stability ($T_{d, 5\%} > 357$ °C), and excellent hydrophobicity and oleophilicity. In addition, these aerogels possess good organic solvent absorption ability and demonstrate high separation efficiency in oil–water separation.

Introduction

Aerogels are a class of three-dimensional porous materials derived by replacing the liquid component of the gel with air. Due to their extremely low density and high porosity, aerogels have unique physical properties such as high specific surface area, low thermal conductivity, and high adsorption capacity [1–6]. Therefore, they have potential applications in a variety of fields such as oil–water separation [7–9], thermal insulators [10–12], energy storage [13, 14], catalysts [15, 16], and space exploration [17]. As the most developed aerogels, silica aerogels have received wide attention due to their low-cost raw materials, relatively facile preparation process, and

Handling Editor: Chris Cornelius.

Address correspondence to E-mail: lei.li@sdu.edu.cn; fsy@sdu.edu.cn

high solvent and thermal resistance properties [18]. However, pristine silica aerogels are brittle and often suffer structural damage due to capillary tension generated during solvent drying process [18]. Hence, supercritical drying process is adopted for most pristine silica aerogels, which restricts their large-scale preparation [19]. In addition, their poor ability to withstand external forces makes them not suitable for load-bearing situations, which greatly limits their applications [20]. Therefore, it is of great importance to develop easily accessible aerogels with ultra-low density and enhanced flexibility.

For the reinforcement and toughening of silica aerogels, different strategies have been developed. One strategy is to introduce various reinforcing components, including polymers [11, 21–26] or organic/inorganic fibers [6, 27–34]. These components interspersed between the skeletons of silica aerogels can effectively improve the compression resistance and flexibility of aerogels. However, these polymers or fibrous components will inevitably fill the pores of aerogels, leading to the increase in densities and decrease in porosities. Another effective strategy is constructing organic–inorganic hybrid aerogels by using organic silane precursors. Compared with silica aerogels derived from tetrafunctional alkoxysilanes, these organic–inorganic hybrid aerogels have a lower Si–O–Si cross-link density, making the aerogels more flexible. These organic groups attached to silica atoms or embedded in the backbone can enhance the elastic recovery of aerogels in compression. For instance, Kanamori et al. reported a flexible aerogel derived from methyltrimethoxysilane and dimethyldimethoxysilane as the co-precursor, which could withstand at least 80% of the compressive deformation and almost completely recovered its original shape and size after unloading the stress [35, 36]. Bridged sesquisiloxanes [37, 38] are a popular class of precursors that can be synthesized through thiol–ene click reaction [39, 40], thiol–isocyanate reaction [41], amino-isocyanate reaction [42], etc. The introduction of organic bridging groups can significantly increase hydrophobicity and oleophilicity while enhancing the flexibility of aerogels, making these aerogels promising candidates for oil–water separation.

Schiff's bases are a class of bridging groups with rich structural variety and are widely used in covalent organic frameworks. But except a bis(propyliminomethyl)benzene moiety [12, 43–45], Schiff's bases are rarely used in the design of sesquisiloxane aerogels. In this work, we prepared 5,5'-methylene-bis-salicylaldimine-bridged aerogels with a vacuum-drying method. 5,5'-Methylene-bis-salicylaldimine was selected due to its facile synthesis via ambient Schiff-base reaction, relative rigid molecular skeleton and enhanced hydrolytic stability resulted from the intramolecular C=N···H–O hydrogen bond interaction. An aerogel with various compositions was prepared by the sol–gel process of this bridged precursor and with methyltriethoxysilane as the co-precursor. The bridged silsesquioxane aerogels exhibit high porosity (> 90%), ultra-low density (0.058 g cm^{-3}), high compression resistance (> 80% strain), good thermal stability ($T_{d, 5\%} > 357$ °C), and excellent hydrophobicity and oleophilicity. Oil–water separation experiments demonstrated that the aerogel could achieve oil–water separation in several ways and with a high separation efficiency.

Materials and methods

Materials

5,5'-Methylene-bis-salicylaldehyde was synthesized as described in the literature [46]. Methyltriethoxysilane and 3-aminopropyltriethoxysilane were purchased from Energy Chemical. Tetrahydrofuran, glacial acetic acid, and anhydrous ethanol were purchased from Tianjin Fuyu Chemical Co., China. All the reagents were used without further purification.

Synthesis of the precursor MSA-TES

5, 5'-Methylene-bis-salicylaldehyde (0.64 mmol) was added to 10 mL of tetrahydrofuran in a 25-mL round-bottom flask and stirred for 5 min, and then, 3-aminopropyltriethoxysilane (1.28 mmol) was added into the mixture. After stirring for another 4 h at room temperature, the solvent was removed by vacuum distillation to obtain the MSA-TES precursor. Yield: ≥ 99%.

Preparation of aerogels

In a typical synthesis, 4 mL ethanol and 0.25 mL tetrahydrofuran were mixed in a beaker, then certain amounts of MSA-TES and methyltriethoxysilane

were added into the above mixture, maintaining the molar concentration of Si atoms fixed at 0.27 mol L^{-1}. After stirring for 10 min at room temperature, 0.3 mL of deionized water and 40 µL of glacial acetic acid were slowly added under stirring conditions. After further stirring for 10 min, the solution was transferred into a sealed cylindrical mold and rested in an oven at 60 °C for 18 h. The resulting wet gel was taken out and immersed in ethanol at 60 °C for 4 h to remove the unreacted components. Finally, the wet gel was dried in a vacuum drying oven at 40 °C for 6 h and then heated at 80 °C to constant weight.

Characterization

^{1}H NMR, ^{13}C NMR, and ^{29}Si NMR spectra were recorded on a Bruker Avance 400 MHz spectrometer (Germany) at 25 °C. Chemical shifts were reported in δ (ppm), and $CDCl_3$ was used as the solvent. Solid-state ^{13}C and ^{29}Si NMR study were performed on a Bruker Avance III 400 MHz cross-polarization/magic-angle spinning (CP-MAS) NMR spectrometer. Fourier transform infrared spectrum (FT-IR) was recorded from the 4000 to 400 cm^{-1} on a Bruker Tensor 27 infrared spectrophotometer (Germany) with the KBr pellet technique. Brunauer–Emmet–Teller (BET) specific surface area was determined by N_2 sorption–desorption measurement with Micromeritics ASAP 2460 analyzer. Mercury intrusion porosimetry (MIP) analysis was carried out using an AutoPore V 9600 instrument to measure the pore size distribution and porosity of aerogels. Scanning electron microscope (SEM) images were taken using a Zeiss G300 field-emission microscope. The apparent density of aerogels was calculated from their mass-to-volume ratios. The shrinkage of aerogels was calculated from the diameter of the gel and dried sample. Thermogravimetric analysis (TGA) was carried out on a Mettler Toledo thermogravimeter SDTA-854 from 40 to 800 °C with a heating rate of 10 °C/min under N_2 flow. Mechanical compression tests of aerogels were conducted on a Instron 3343 material testing system with a strain rate of 1 mm/min. The surface wettability of aerogels was tested by a Dataphysics OCA20 contact angle analyzer.

Results and discussion

Synthesis of the precursor

As shown in Scheme 1, the imine-bridged precursor MSA-TES was obtained via the Schiff-base reaction between 5,5′-methylene-bis-salicylaldehyde (MSA) and 3-aminopropyltriethoxysilane (APTES) at room temperature. The ^{1}H, ^{13}C, and ^{29}Si NMR spectra of MSA-TES are shown, respectively, in Fig. 1. The ^{1}H NMR spectrum (Fig. 1a) shows that the amino proton peak of APTES (δ = 1.34–1.37 ppm) and the aldehyde proton peak of MSA (δ = 9.83–9.86 ppm) have disappeared after the reaction, and the resonance signal of the imine proton appears at 8.25–8.27 ppm. In addition, the integrated ratio of each proton peak is {(a,b,c,d,e):(f,g,h):i:j = 1:2:6:9}, which is in agreement with the theoretical calculated value. According to the ^{13}C NMR spectrum of the precursor (Fig. 1b), the characteristic signal of the carbons of the imine group appears at 159.4 ppm, and the chemical shifts of all the other resonance peaks are consistent with the structure of the precursor. Figure 1c shows the ^{29}Si NMR spectrum of the precursor, where only one strong resonance signal appears at δ = − 45.7 ppm in accordance with the triethoxysilane structure in the product. The FT-IR spectra of the two raw materials APTES, MSA and MSA-TES are presented in Fig. 2. After the reaction of APTES with MSA, the peak of the amino group at 3350 cm^{-1} and that of the aldehyde group at 1654 cm^{-1} disappeared, accompanied by the appearance of a new absorption of imine group at 1635 cm^{-1}, indicating the high reaction efficiency. All these results demonstrate that the bridging precursor was successfully synthesized via the mild Schiff-base reaction.

Chemical structure of the aerogels

With the silane precursor in hand, the imine-bridged silica aerogel was prepared by the acid-catalyzed hydrolysis and condensation of MSA-TES, where the solvent was easily removed via a vacuum drying process. Methyltriethoxysilane was also used as a co-monomer in the sol–gel process in order to tune the structures of obtained aerogels. By adjusting the molar ratio between MSA-TES and methyltriethoxysilane, three kinds of aerogels were obtained and named as A100-0 (100 mol% of MSA-TES), A80-20 (80 mol% of MSA-TES and 20 mol% of

Scheme 1 a Synthesis of the MSA imine-bridged precursor. **b** Preparation procedure of aerogels.
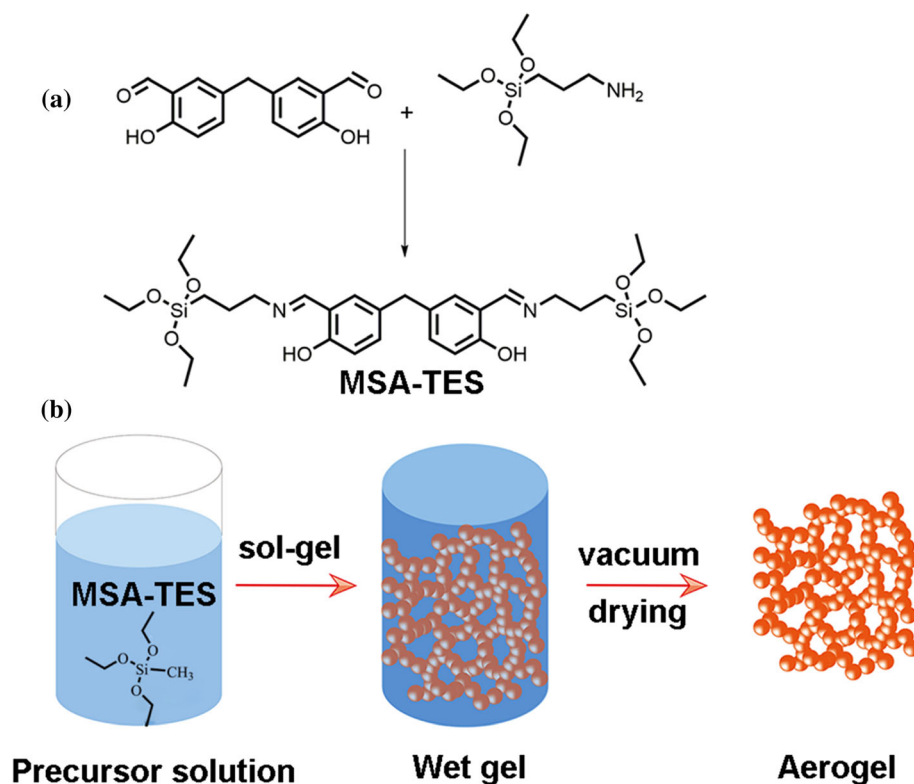
methyltriethoxysilane), and A70-30 (70 mol% of MSA-TES and 30 mol% of methyltriethoxysilane), respectively. FT-IR spectrum of A100-0 in Fig. 2 reveals that the absorption band at 1636 cm^{-1} characteristic of imine groups remains intact after the sol–gel process, proving that the acid-catalyzed process does not lead to observable degradation of the imine structure. The absorption band of the aerogel sample at 1000–1100 cm^{-1} splits into two strong peaks, which marks the formation of Si–O–Si structure by the condensation of Si–OH groups. The peaks around 3400 cm^{-1} can be attributed to residual Si–OH groups, indicating the incomplete condensation of Si–OH groups during the gelation process. For further analyzing the chemical structure of the bridged aerogel, sample A80-20 was characterized with ^{13}C and ^{29}Si CP-MAS NMR, and the obtained spectra are shown in Fig. 3. The ^{13}C NMR result (Fig. 3a) shows that the aerogel A80-20 has the characteristic signals of 5,5′-methylene-bis-salicylaldimine and methyl silane groups generated from the precursors MSA-TES and methyltriethoxysilane, demonstrating the intactness of the bridging skeletons in the aerogel. The absence of resonance signal of –OCH$_2$CH$_3$ indicates that both precursors were totally hydrolyzed into silanol compounds. The ^{29}Si solid-state NMR

spectrum shows two peaks located at − 59.8 ppm and − 67.6 ppm, attributed to silicon atom signals of T^2 (R–Si(OSi)$_2$OH) and T^3 (R–Si(OSi)$_3$) units, respectively. The T^2 units are the result of the incomplete condensation between the Si–OH groups. More importantly, the absence of any silicon atom signals from (Si(OSi)$_i$(OH)$_{4-i}$)-like units (about-120– 80 ppm) means that no cleavage of Si–C bonds occurs in the sol–gel process. The above results clearly demonstrate that the aerogels with 5,5′-methylene-bis-salicylaldimine groups have been successfully prepared.

Physical structure and thermal properties

Representative photographs of three aerogels are shown in Fig. 4a. Compared with the conventional silica aerogels that undergo large volume shrinkage (> 20%) [19] or structural collapse [18] after the drying process, the volume shrinkage of the three aerogels in this system is relatively small. On one hand, these aerogels with large pore sizes are subjected to less capillary force during the solvent drying process. On the other hand, the high content of organic components and the relative flexible skeleton improve their resistance to the capillary forces. According to the results in Table 1, increasing the ratio of
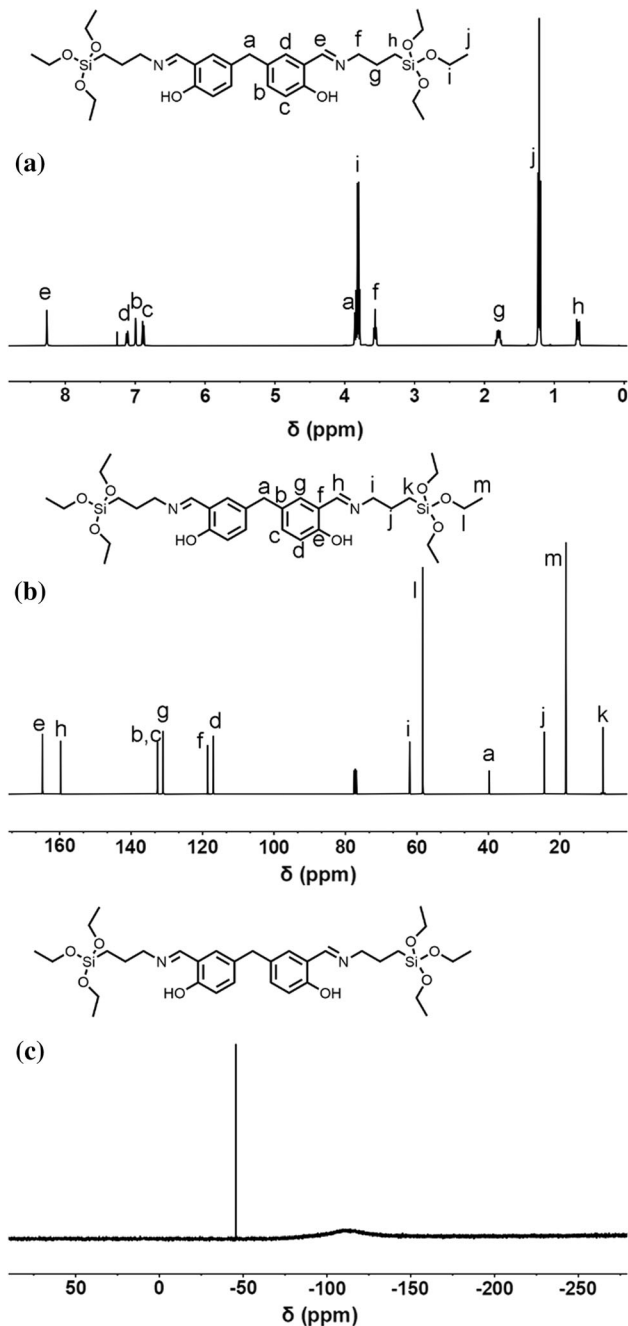
Figure 1 a ^{1}H NMR, b ^{13}C NMR, and c ^{29}Si NMR spectra of the precursor MSA-TES.

Figure 2 FT-IR spectra of APTES, MSA, MSA-TES, and aerogel A100-0.
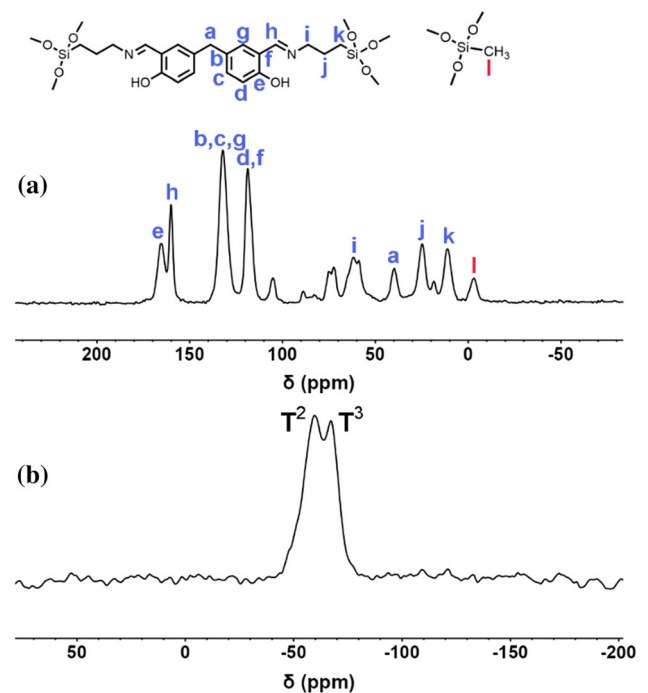
Figure 3 ^{13}C and ^{29}Si CP-MAS NMR spectra of aerogel A80-20.

methyltriethoxysilane significantly reduced the volume shrinkage of aerogels. As we mentioned above, the condensation of silica hydroxyl groups during the gelation of aerogels was incomplete, and many residual Si–OH groups remained on the surface of the colloidal particles. During solvent volatilization, colloidal particles aggregated under capillary pressure and simultaneously underwent inter-particle Si–OH
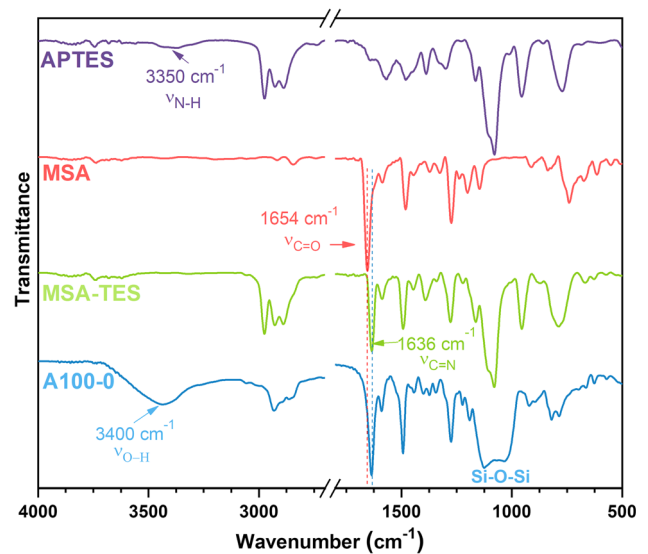
condensation, resulting in inter-particle cross-linking and exhibiting permanent volume shrinkage. With the addition of methyltriethoxysilane, the flexible Si–CH$_3$ group was enriched on the particle surface and improved the hydrophobicity of the particle surface. These hydrophobic silicone methyl groups inhibited the inter-particle condensation of silanols during solvent evaporation, allowing the aerogel to spring
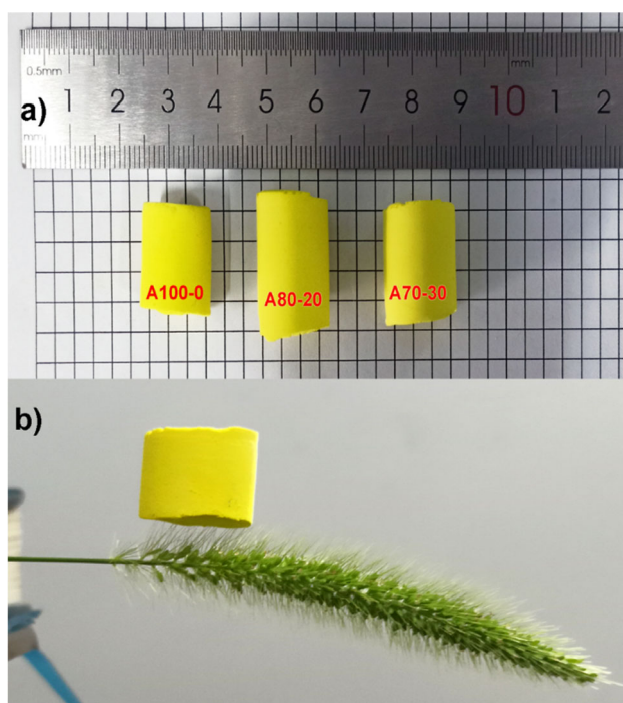
Figure 4 a Representative photographs of A100-0, A80-20, and A70-30. **b** Sample A70-30 on green bristlegrass.

back after the drying process, thus significantly reduced the permanent volume shrinkage of A80-20 and A70-30. The excellent volume retention capability endows these aerogels with relatively low apparent densities (Fig. 4b), which will facilitate their performance in a variety of applications.

The morphologies of aerogels were investigated by SEM, and the results are shown in Fig. 5. All aerogels have a skeleton network with a typical pearl-necklace-type morphology. This skeletal network was formed by the random stacking and fusion of colloidal particles of different diameters. This aggregation and fusion process can be clearly seen in the magnified image (Fig. 5d–f). Figure 5g–i shows the size distribution of colloidal particles for the three aerogels, with average particle diameters of 0.73, 0.84, and 0.89 μm for A100-0, A80-20, and A70-30,

respectively. Particles of this larger size build a more robust aerogel skeleton compared with thioether [40] or alkylene [37] bridged silsesquioxane aerogels. In addition, the particles were closely packed, and there was a high degree of fusion between adjacent particles, which made the "neck" of the pearl-necklace not clearly distinguishable. Because the necks are considered to be the vulnerability points for silica aerogels, this high degree of fusion herein helps to improve the mechanical strength of obtained aerogels.

The porous structure of obtained aerogels was quantitatively analyzed by nitrogen adsorption–desorption experiments and mercury intrusion porosimetry (MIP). As shown in Fig. 6a, all the N_2 adsorption–desorption isotherms of three aerogels show the type III plots according to IUPAC classification, indicating their macroporous structures. Brunauer–Emmet–Teller (BET) surface areas of A100-0, A80-20, and A70-30 are 17.8, 12.4, and 14.9 m^2 g^{-1}, respectively. According to the MIP analysis, the porosity values of these three aerogels are higher than 90%. The pressurization curves in Fig. 6b–d show that the critical pressure P_c [45, 47] of aerogels A100-0, A80-20, and A70-30 is 16, 16, and 110 kPa, respectively. According to the Washburn equation [48], the pore diameter is inversely proportional to the mercury intrusion pressure. Therefore, according to the relationship between mercury intrusion volume and pressure on the mercury intrusion curves, the relationship between pore volume and pore diameter can be obtained, i.e., the pore size distribution curves, which were inserted in Fig. 6b–d. The pore size distribution curves outline that pore sizes of A100-0, A80-20, and A70-30 distribute in the range of 7.2–13.9 μm, 6.0–13.9 μm, and 5.5–13.5 μm, respectively.

The thermal stability of aerogels was characterized by TGA under nitrogen atmosphere. The temperatures at 5% weight loss for A100-0, A80-20, and A70-

Table 1 Physical properties of the aerogels

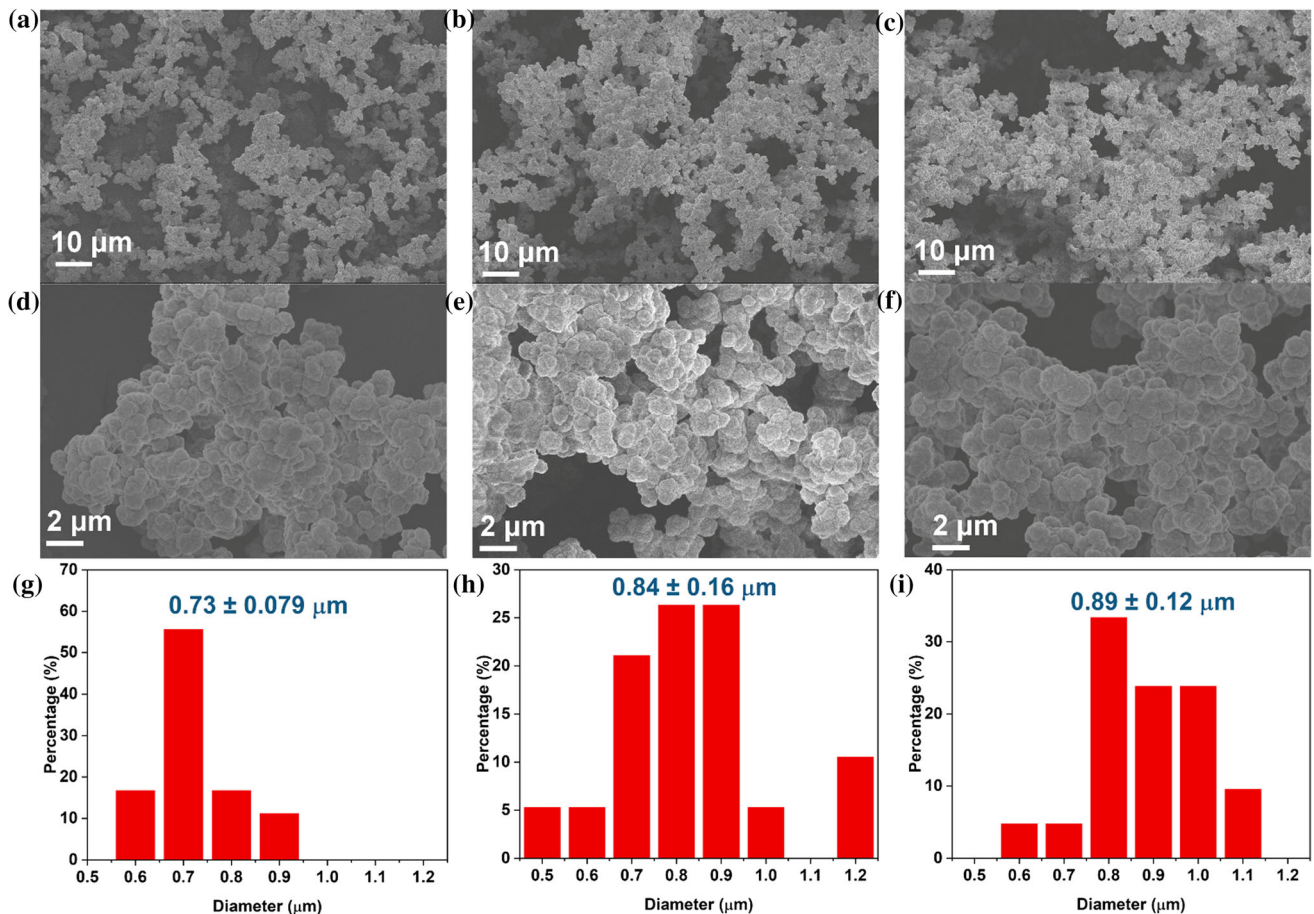| Samples	Apparent density (g cm^{-3})	Volume shrinkage (%)	BET specific surface area (m^2 g^{-1})	Porosity (%)	Young's modulus (MPa)	Temperature for the 5% weight loss (°C)
A100-0	0.074 ± 0.002	9.37 ± 0.35	17.8 ± 0.12	90.5 ± 0.6	0.059 ± 0.009	357
A80-20	0.062 ± 0.003	3.13 ± 0.18	12.4 ± 0.06	91.7 ± 0.8	0.030 ± 0.003	360
A70-30	0.058 ± 0.002	2.50 ± 0.15	14.9 ± 0.10	92.7 ± 0.3	0.031 ± 0.003	362

Figure 5 SEM images of aerogels: **a,d** A100-0, **b,e** A80-20, **c,f** A70-30 and size distribution of aerogels: **g** A100-0, **h** A80-20, **i** A70-30.

30 were 357 °C, 360 °C, and 362 °C, respectively, which demonstrated that these aerogels have excellent thermal stability. In the TG-DTG curves (Fig. 7), two obvious weight loss stages in the temperature range of 305–440 °C and 440–600 °C can be attributed to the decomposition of the organic bridging groups and siloxane bonds, respectively. In addition, the trace weight loss below 200 °C is believed to be the evaporation of H_2O generated from further condensations of residual Si–OH groups.

Mechanical properties

The mechanical property of aerogel is an important aspect in almost all applications, especially in oil–water separation, where the resistance to repeated compression and the deformation recovery ability are highly required. Therefore, we investigated their mechanical properties via axial compression experiments. All aerogel samples can withstand at least 80% compressive deformation without damage and

recover to more than 95% of their original size after the removal of external force for 30 min (Fig. 8a). Figure 8b shows the cyclic stress–strain curves of A100-0, A80-20, and A70-30 obtained from axial compression experiments at 70% compressive deformation. At 70% compressive deformation, the compressive stresses of aerogels A100-0, A80-20, and A70-30 reached 0.33, 0.20 and 0.17 MPa, respectively. The relatively low stresses reflect that these aerogels are very flexible, which will effectively reduce the applied energy in the compression applications. Moreover, no rupture, collapse, or crushing of these aerogels occurred in the compression process, even though this kind of structural damage phenomenon was quite common for compressing unmodified silica aerogels. This result indicates that the introduction of the bridging group has effectively improved the compression resistance of the aerogel.

To verify the deformation recovery ability of aerogels during repeated compression, 10 consecutive cyclic compression tests with the maximum
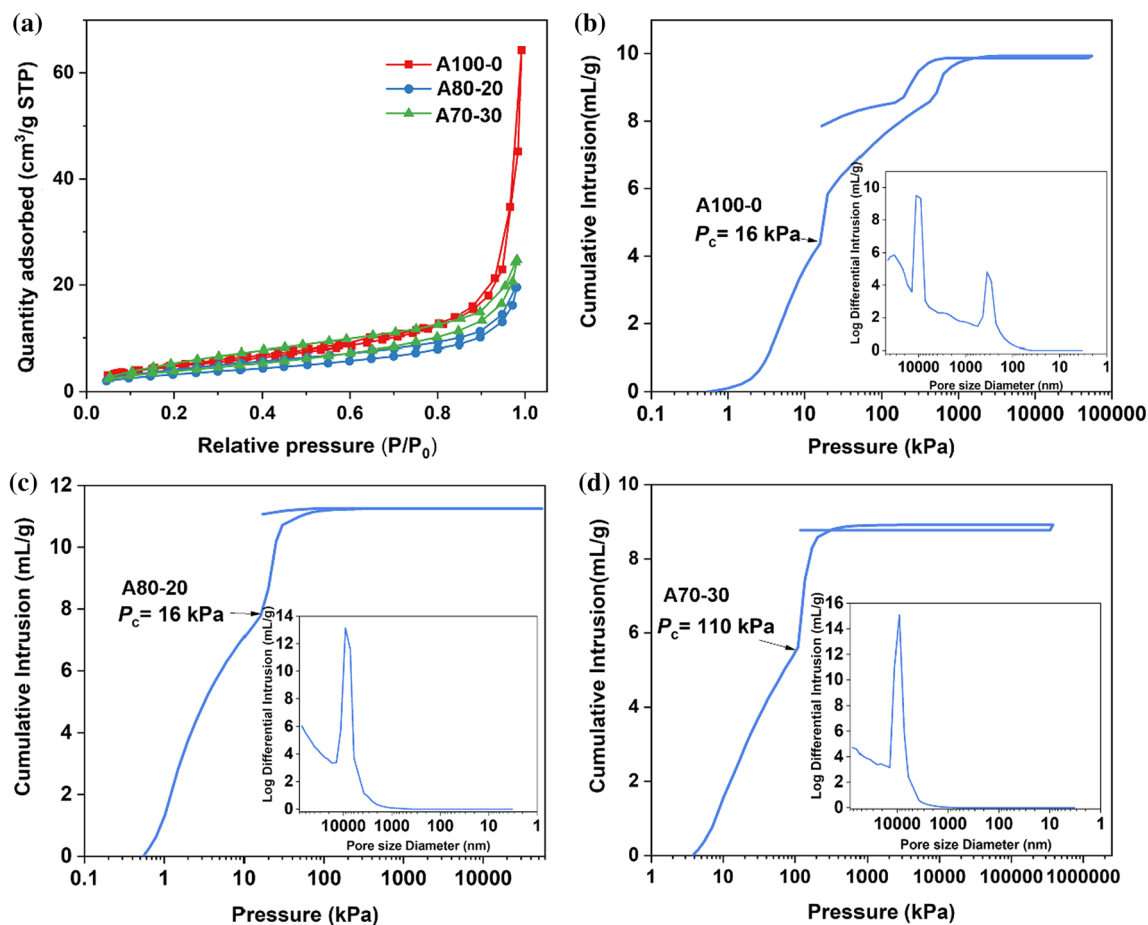
Figure 6 **a** N_2 adsorption and desorption isotherms of the aerogels. Mercury intrusion and extrusion curves of **b** A100-0, **c** A80-20, and **d** A70-30; the insert figures are the pore size distribution curves obtained by MIP analysis.

deformation at 50% were applied (Fig. 8c–e). After the first compression, the time is not sufficient for the aerogels to totally restore their original size. Therefore, a horizontal line without stress appears at the initial stage of the compression curve, the length of which also represents the magnitude of the plastic deformation after the compression. From aerogels A100-0, A80-20 to A70-30, the plastic deformation is less significant, because that the molecular interactions inside aerogels are much weaker with the increase in less polar Si–CH$_3$ content. Moreover, the stress at 50% compression strain remains constant with the increase in compression cycles, further confirming the capability of these aerogels in resisting structural damage during compression.

Wettability

The surface wettability of aerogels is another important parameter in oil–water separation applications,

which directly affects the absorbency of organic solvents and the oil–water separation efficiency. All three aerogels exhibited good hydrophobic properties (Fig. 9a), despite the fact that a portion of Si–OH groups remained inside the aerogels. After completely submerging in water and taking out, the surface of aerogels remains completely dry. The static water contact angles of aerogels A100-0, A80-20 and A70-30 are 137°, 148° and 150°, respectively. As expected, the increase in Si-CH$_3$ content enhanced the hydrophobic properties of aerogels. In addition, the water contact angles on the aerogel surface and cross section are consistent, indicating the homogenous nature of these aerogels. Figure 9b shows the result of water droplet adhesion experiment of aerogel A70-30. The aerogel surface was placed in contact with the water droplet, held for 10 s, and then moved downward. In this process, the water droplet remained almost spherical and adhered to the syringe all the time without losing any mass, which nicely
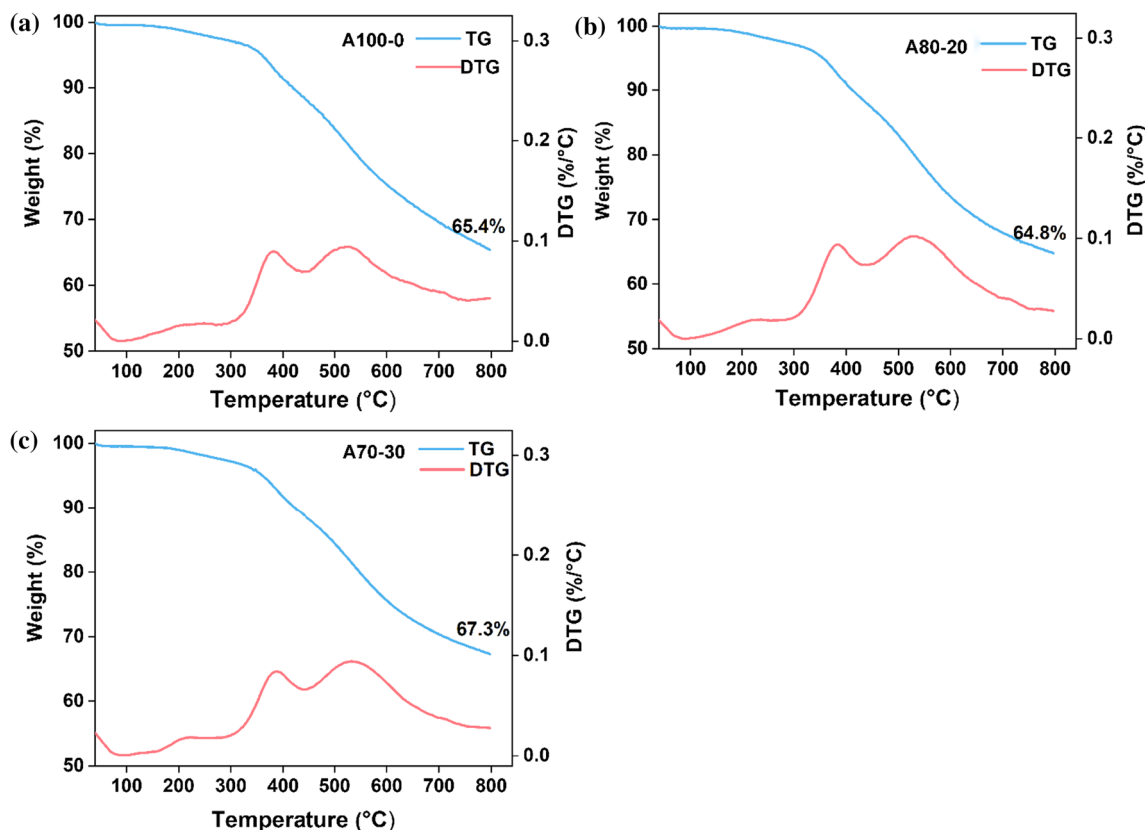
Figure 7 TG-DTG curves of **a** A100-0, **b** A80-20, and **c** A70-30.

demonstrated the excellent water repellency of aerogel A70-30. To further test the oleophilicity and oil absorption ability of aerogels, we chose n-hexane, a common petroleum fraction, as the representative oil substance. All three aerogels exhibit good oleophilicity, and n-hexane droplets quickly enter the inner pores once they come into contact with the aerogels, leaving only dyed oil stains on the surface (Fig. 9c). It can be concluded that this series of aerogels exhibit excellent hydrophobic and oleophilic properties, which will be helpful for their applications in oil–water separation.

Oil–water separation applications

Considering the fact that these aerogels possess hydrophobic and oleophilic properties and exhibit good flexibility during the repeated compression process, they are expected to be valuable for oil–water separation applications. The obtained aerogels were immersed in various organic solvents and taken out after 5 min, and their absorption capacities of different solvents were measured by testing the mass ratio after and before the adsorption. Due to the good oleophilicity of aerogels, rapid absorption saturation occurred within 5 min. The absorption capacities of each aerogel for various organic solvents are shown in Fig. 10a and vary roughly in the same trend. Thanks to their more hydrophobic and oleophilic nature, the oil absorption capacities of aerogels A80-20 and A70-30 are much higher than that of A100-0. In order to extract absorbed oils from adsorptive materials, mechanical squeezing and gravity-driven separation are undoubtedly more eco-friendly and energy-saving in comparison with other methods like oil evaporation or solvent washing. Since aerogels have good compression resistance, we first tested the repeated absorption-squeezing-reabsorption capability to hexane of aerogel A70-30. The aerogel was soaked in n-hexane for 5 min and then squeezed to release the hexane. The masses of the aerogel after saturation absorption and after being squeezed in each cycle are recorded, as displayed in Fig. 10b. During the first cycle, the saturated absorption of hexane is 10 g/g, and the remaining absorption after squeezing is 4 g/g. During the succeeding cycles, the
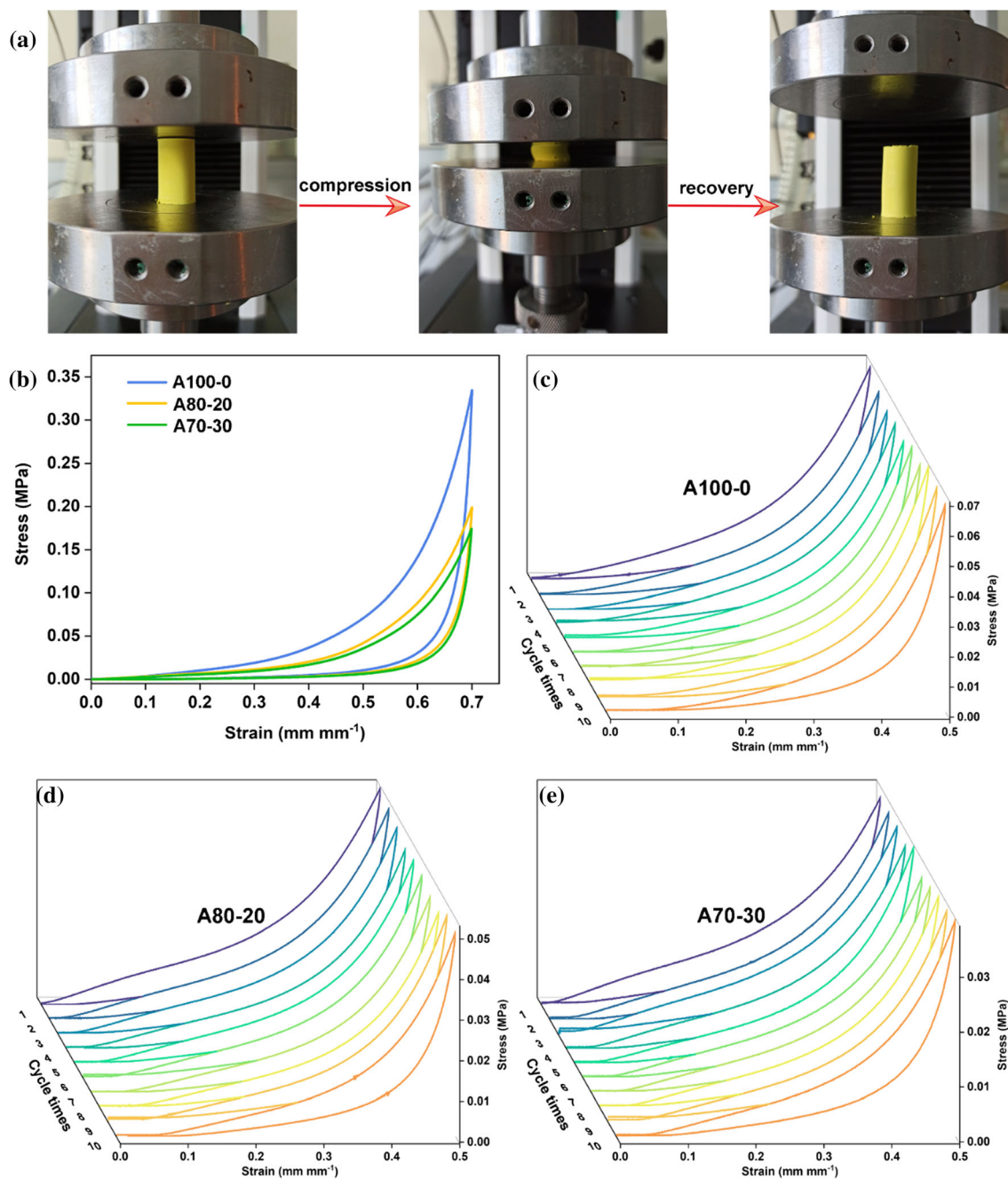
Figure 8 Compressive stress—strain curves of the aerogels. **a** The compression and spring back behavior of A70-30. **b** Cyclic stress–strain curves of A100-0, A80-20, and A70-30 at 70% compressive deformation. **c**–**e** 10-time-repeated compression tests of the aerogels.

saturated absorption and the extruded residual mass decreased slightly and then remained stable, indicating the robust reusability of the aerogel in the oil absorption-squeezing cycles.

With n-hexane as an example, we simulated the absorption of floating oil on the water surface, as shown in Fig. 10c. For easy observation, hexane and water were stained with methyl red and methylene blue, respectively. When a piece of aerogel A70-30 was contacted with the liquid, the aerogel floated on the water surface and quickly soaked up the n-hexane, leaving a clean water surface with no residual floating oil. The hexane absorbed by the aerogel was squeezed out and collected in another container, and no water droplet could be observed in the collected hexane. The separation efficiency of aerogel for water
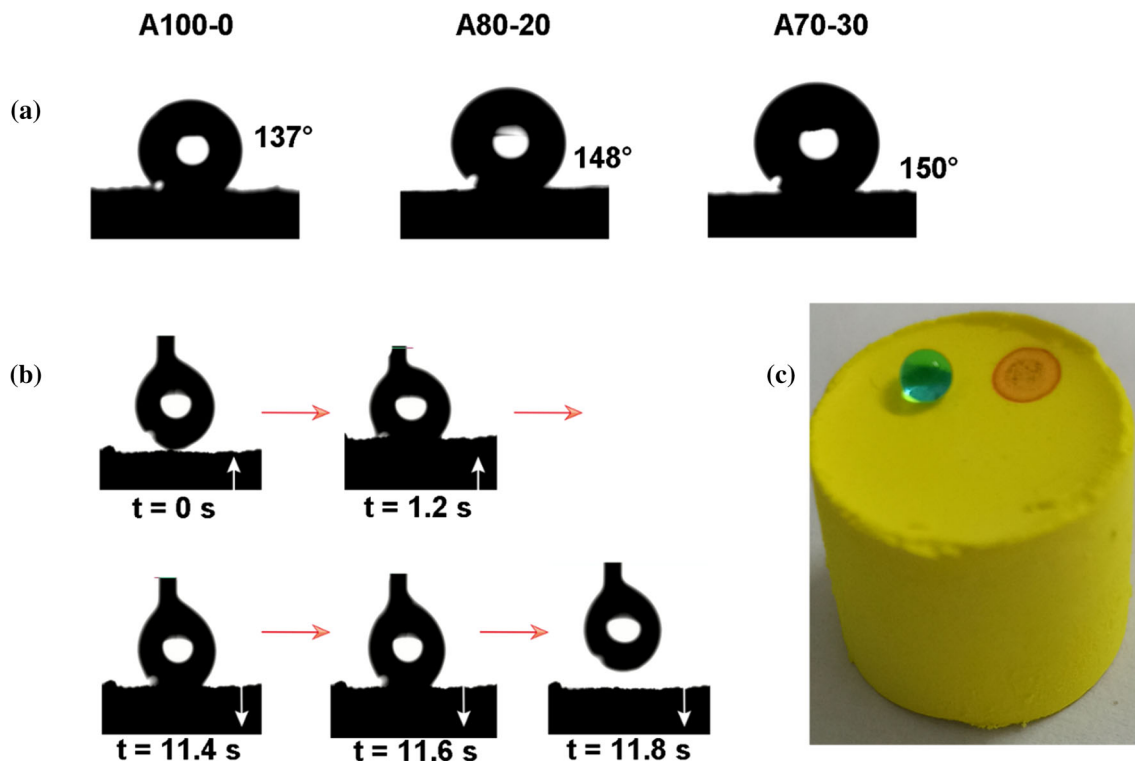
Figure 9 The surface wettability of aerogels. **a** Water contact angle data of the aerogels. **b** Images of A70-30 moves upward until it touches the water droplet, hold for 10 s, then moves downward until it leaves the water droplet. **c** Images of A70-30 with the droplet of water (blue) and n-hexane (red).

and hexane was evaluated by the mass ratio of water after and before oil absorption, which was as high as 99.2%.

As shown in Fig. 10d, we further verified the gravity-driven oil–water separation effect of the aerogel A70-30 for high-density organic solvents. The aerogel was filled at the bottom of the syringe. Thanks to the flexible property, the aerogel fitted tightly into the syringe without leaving any gap. Then, the mixture of dichloromethane and water was poured into the syringe. Since the aerogel repels water, water molecules could not pass through the aerogel layer, while dichloromethane could continuously pass under the drive of gravity, resulting in the complete separation of water and dichloromethane. All these results demonstrate the great potential of these aerogels for oil–water separation applications. It must be emphasized that imine bonds are susceptible to strong acidic environments. As previously reported [49, 50], the salicylaldimine structure is stable at pH > 4, but at pH < 4, the imine bond is hydrolyzed and salicylaldehyde is released. This phenomenon is useful for controlled drug release, but in oil–water separation applications, the hydrolysis under acidic conditions can cause the disintegration of aerogels. Therefore, these aerogels are not suitable for oil–water separation of strongly acidic wastewater, or should be used after neutralizing the strong acid.

Conclusions

In summary, we designed and prepared a series of flexible 5,5′-methylene-bis-salicylaldimine-bridged silsesquioxane aerogels. The bridged precursor was synthesized via a facile ambient Schiff-base reaction and used to prepare bridged aerogels through sol–gel process with methyltriethoxysilane as the co-precursor. Thanks to their toughened skeleton and macroporous structure, the aerogels could be prepared through a facile vacuum drying method. The obtained aerogels exhibit high porosity, ultra-low density, high compression resistance, and excellent hydrophobicity and oleophilicity. These outstanding properties enable the aerogels to perform well in oil–water separation applications.
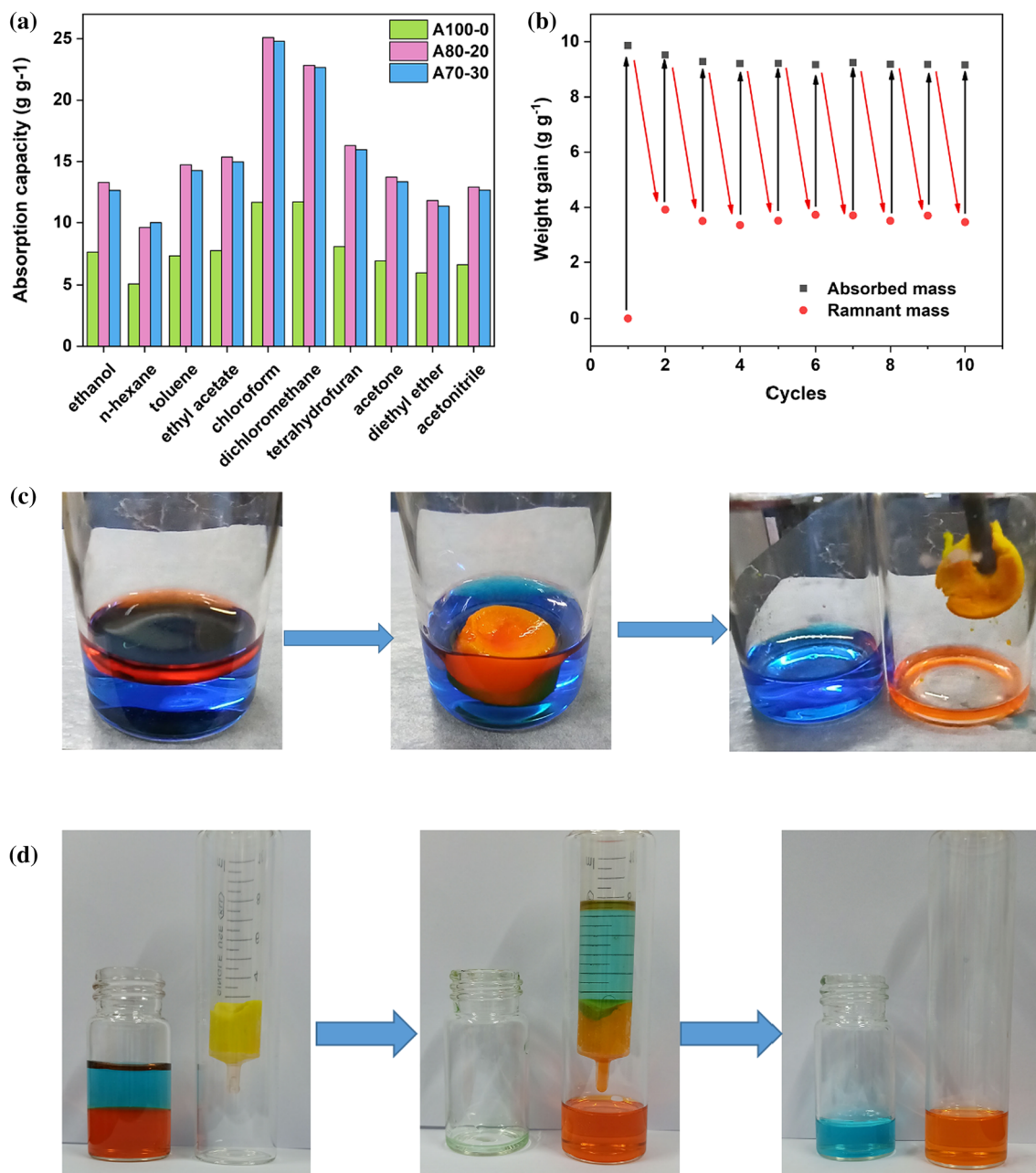
Figure 10 **a** Absorption capacities of A100-0, A80-20, and A70-30 for various organic liquids. **b** Absorption capacities of A70-30 for n-hexane in repeated absorption-squeezing cycles. **c** Separation of n-hexane from water with A70-30. **d** Gravity-driven separation of dichloromethane from water. Organic liquids were stained with methyl red and water was stained with methylene blue for observation.

Declarations

Conflict of interest The authors declare that they have no known competing financial interest or

personal relationships that could have appeared to influence the work reported in this paper.

References

[1] Kistler SS (1931) Coherent expanded aerogels and jellies. Nature 127:741. https://doi.org/10.1038/127741a0

[2] Hüsing N, Schubert U (1998) Aerogels—airy materials: chemistry, structure, and properties. Angew Chemie Int Ed 37:22–45. https://doi.org/10.1002/(SICI)1521-3773(19980202)37:1/2%3c22::AID-ANIE22%3e3.0.CO;2-I

[3] Pierre AC, Pajonk GM (2002) Chemistry of aerogels and their applications. Chem Rev 102:4243–4266. https://doi.org/10.1021/cr0101306

[4] Aegerter M, Leventis N, Koebel M (2011) Aerogels handbook (Advances in Sol-Gel Derived Materials and Technologies) Springer, New York

[5] Liu Z, Lyu J, Fang D, Zhang X (2019) Nanofibrous kevlar aerogel threads for thermal insulation in harsh environments. ACS Nano 13:5703–5711. https://doi.org/10.1021/acsnano.9b01094

[6] Almeida CMR, Ghica ME, Ramalho AL, Durães L (2021) Silica-based aerogel composites reinforced with different aramid fibres for thermal insulation in space environments. J Mater Sci 56:13604–13619. https://doi.org/10.1007/s10853-021-06142-3

[7] Yang X, Cranston ED (2014) Chemically cross-linked cellulose nanocrystal aerogels with shape recovery and superabsorbent properties. Chem Mater 26:6016–6025. https://doi.org/10.1021/cm502873c

[8] Dai J, Zhang R, Ge W et al (2018) 3D macroscopic superhydrophobic magnetic porous carbon aerogel converted from biorenewable popcorn for selective oil-water separation. Mater Des 139:122–131. https://doi.org/10.1016/j.matdes.2017.11.001

[9] Zhao Y, Zhong K, Liu W et al (2020) Preparation and oil adsorption properties of hydrophobic microcrystalline cellulose aerogel. Cellulose 27:7663–7675. https://doi.org/10.1007/s10570-020-03309-0

[10] Huber L, Zhao S, Malfait WJ et al (2017) Fast and minimal-solvent production of superinsulating silica aerogel granulate. Angew Chemie Int Ed 56:4753–4756. https://doi.org/10.1002/anie.201700836

[11] Zu G, Shimizu T, Kanamori K et al (2018) Transparent, superflexible doubly cross-linked polyvinylpolymethylsiloxane aerogel superinsulators via ambient pressure drying. ACS Nano 12:521–532. https://doi.org/10.1021/acsnano.7b07117

[12] Zhao Z, Cui Y, Kong Y et al (2021) Thermal and mechanical performances of the superflexible, hydrophobic, silica-based aerogel for thermal insulation at ultralow temperature. ACS Appl Mater Interfaces 13:21286–21298. https://doi.org/10.1021/acsami.1c02910

[13] Lin Z, Zeng Z, Gui X et al (2016) Carbon nanotube sponges, aerogels, and hierarchical composites: synthesis, properties, and energy applications. Adv Energy Mater 6:1600554. https://doi.org/10.1002/aenm.201600554

[14] Li D, Yang D, Yang X et al (2016) Double-helix structure in carrageenan-metal hydrogels: a general approach to porous metal sulfides/carbon aerogels with excellent sodium-ion storage. Angew Chemie Int Ed 55:15925–15928. https://doi.org/10.1002/anie.201610301

[15] Qiu B, Xing M, Zhang J (2014) Mesoporous TiO 2 nanocrystals grown in situ on graphene aerogels for high photocatalysis and lithium-ion batteries. J Am Chem Soc 136:5852–5855. https://doi.org/10.1021/ja500873u

[16] Sanz-Moral LM, Aho A, Kumar N et al (2018) Synthesis and characterization Ru–C/SiO2 aerogel catalysts for sugar hydrogenation reactions. Catal Lett 148:3514–3523. https://doi.org/10.1007/s10562-018-2556-4

[17] Randall JP, Meador MAB, Jana SC (2011) Tailoring mechanical properties of aerogels for aerospace applications. ACS Appl Mater Interfaces 3:613–626. https://doi.org/10.1021/am200007n

[18] Maleki H, Durães L, Portugal A (2014) An overview on silica aerogels synthesis and different mechanical reinforcing strategies. J Non Cryst Solids 385:55–74. https://doi.org/10.1016/j.jnoncrysol.2013.10.017

[19] Linhares T, Pessoa de Amorim MT, Durães L (2019) Silica aerogel composites with embedded fibres: a review on their preparation, properties and applications. J Mater Chem A 7:22768–22802. https://doi.org/10.1039/C9TA04811A

[20] Lin J, Li G, Liu W et al (2021) A review of recent progress on the silica aerogel monoliths: synthesis, reinforcement, and applications. J Mater Sci 56:10812–10833. https://doi.org/10.1007/s10853-021-05997-w

[21] Zu G, Kanamori K, Maeno A et al (2018) Superflexible multifunctional polyvinylpolydimethylsiloxane-based aerogels as efficient absorbents, thermal superinsulators, and strain sensors. Angew Chemie Int Ed 57:9722–9727. https://doi.org/10.1002/anie.201804559

[22] Zu G, Kanamori K, Shimizu T et al (2018) Versatile double-cross-linking approach to transparent, machinable, supercompressible, highly bendable aerogel thermal superinsulators. Chem Mater 30:2759–2770. https://doi.org/10.1021/acs.chemmater.8b00563

[23] Maleki H, Durães L, Portugal A (2015) Synthesis of mechanically reinforced silica aerogels via surface-initiated

reversible addition-fragmentation chain transfer (RAFT) polymerization. J Mater Chem A 3:1594–1600. https://doi.org/10.1039/C4TA05618C

[24] Leventis N, Sotiriou-Leventis C, Zhang G, Rawashdeh A-MM (2002) Nanoengineering strong silica aerogels. Nano Lett 2:957–960. https://doi.org/10.1021/nl025690e

[25] Leventis N (2007) Three-dimensional core-shell superstructures: mechanically strong aerogels. Acc Chem Res 40:874–884. https://doi.org/10.1021/ar600033s

[26] Xi S, Wang X, Liu T et al (2021) Moisture-resistant and mechanically strong polyimide-polymethylsilsesquioxane hybrid aerogels with tunable microstructure. Macromol Mater Eng 306:2000612. https://doi.org/10.1002/mame.202000612

[27] Bhuiyan MAR, Wang L, Shaid A et al (2020) Silica aerogel-integrated nonwoven protective fabrics for chemical and thermal protection and thermophysiological wear comfort. J Mater Sci 55:2405–2418. https://doi.org/10.1007/s10853-019-04203-2

[28] He S, Cheng X, Li Z et al (2016) Green and facile synthesis of sponge-reinforced silica aerogel and its pumping application for oil absorption. J Mater Sci 51:1292–1301. https://doi.org/10.1007/s10853-015-9427-9

[29] Li X, Wang Q, Li H et al (2013) Effect of sepiolite fiber on the structure and properties of the sepiolite/silica aerogel composite. J Sol-Gel Sci Technol 67:646–653. https://doi.org/10.1007/s10971-013-3124-4

[30] Zhao S, Malfait WJ, Demilecamps A et al (2015) Strong, thermally superinsulating biopolymer-silica aerogel hybrids by cogelation of silicic acid with pectin. Angew Chemie Int Ed 54:14282–14286. https://doi.org/10.1002/anie.201507328

[31] Zhao S, Malfait WJ, Jeong E et al (2016) Facile one-pot synthesis of mechanically robust biopolymer-silica nanocomposite aerogel by cogelation of silicic acid with chitosan in aqueous media. ACS Sustain Chem Eng 4:5674–5683. https://doi.org/10.1021/acssuschemeng.6b01574

[32] Maleki H, Whitmore L, Hüsing N (2018) Novel multifunctional polymethylsilsesquioxane–silk fibroin aerogel hybrids for environmental and thermal insulation applications. J Mater Chem A 6:12598–12612. https://doi.org/10.1039/C8TA02821D

[33] Chakraborty S, Pisal AA, Kothari VK, Venkateswara Rao A (2016) Synthesis and characterization of fibre reinforced silica aerogel blankets for thermal protection. Adv Mater Sci Eng 2016:1–8. https://doi.org/10.1155/2016/2495623

[34] Li Z, Cheng X, He S et al (2016) Aramid fibers reinforced silica aerogel composites with low thermal conductivity and improved mechanical performance. Compos Part A Appl Sci Manuf 84:316–325. https://doi.org/10.1016/j.compositesa.2016.02.014

[35] Hayase G, Kanamori K, Nakanishi K (2011) New flexible aerogels and xerogels derived from methyltrimethoxysilane/dimethyldimethoxysilane co-precursors. J Mater Chem 21:17077. https://doi.org/10.1039/c1jm13664j

[36] Hayase G, Kanamori K, Fukuchi M et al (2013) Facile synthesis of marshmallow-like macroporous gels usable under harsh conditions for the separation of oil and water. Angew Chemie Int Ed 52:1986–1989. https://doi.org/10.1002/anie.201207969

[37] Aoki Y, Shimizu T, Kanamori K et al (2017) Low-density, transparent aerogels and xerogels based on hexylene-bridged polysilsesquioxane with bendability. J Sol-Gel Sci Technol 81:42–51. https://doi.org/10.1007/s10971-016-4077-1

[38] Kanamori K, Ueoka R, Kakegawa T et al (2019) Hybrid silicone aerogels toward unusual flexibility, functionality, and extended applications. J Sol-Gel Sci Technol 89:166–175. https://doi.org/10.1007/s10971-018-4804-x

[39] Wang Z, Dai Z, Wu J et al (2013) Vacuum-dried robust bridged silsesquioxane aerogels. Adv Mater 25:4494–4497. https://doi.org/10.1002/adma.201301617

[40] Wang Z, Wang D, Qian Z et al (2015) Robust superhydrophobic bridged silsesquioxane aerogels with tunable performances and their applications. ACS Appl Mater Interfaces 7:2016–2024. https://doi.org/10.1021/am5077765

[41] Zou F, Yue P, Zheng X et al (2016) Robust and superhydrophobic thiourethane bridged polysilsesquioxane aerogels as potential thermal insulation materials. J Mater Chem A 4:10801–10805. https://doi.org/10.1039/c6ta03531k

[42] Zhang Y, Wang J, Wei Y, Zhang X (2017) Robust urethane-bridged silica aerogels available for water-carved aerosculptures. New J Chem 41:1953–1958. https://doi.org/10.1039/C6NJ03414D

[43] Chen D, Gao H, Jin Z et al (2018) Vacuum-dried synthesis of low-density hydrophobic monolithic bridged silsesquioxane aerogels for oil/water separation: effects of acid catalyst and its excellent flexibility. ACS Appl Nano Mater 1:933–939. https://doi.org/10.1021/acsanm.7b00328

[44] Chen D, Dong K, Gao H et al (2019) Vacuum-dried flexible hydrophobic aerogels using bridged methylsiloxane as reinforcement: performance regulation with alkylorthosilicate or alkyltrimethoxysilane co-precursors. New J Chem 43:2204–2212. https://doi.org/10.1039/C8NJ04038A

[45] Chen D, Gao H, Liu P et al (2019) Directly ambient pressure dried robust bridged silsesquioxane and methylsiloxane aerogels: effects of precursors and solvents. RSC Adv 9:8664–8671. https://doi.org/10.1039/C8RA08646J

[46] Marvel CS, Tarköy N (1957) Heat stability studies on chelates from schiff bases of salicylaldehyde derivatives 1. J Am

Chem Soc 79:6000–6002. https://doi.org/10.1021/ja01579a041

[47] Rao AP, Rao AV, Pajonk GM (2005) Hydrophobic and physical properties of the two step processed ambient pressure dried silica aerogels with various exchanging solvents. J Sol-Gel Sci Technol 36:285–292. https://doi.org/10.1007/s10971-005-4662-1

[48] Washburn EW (1921) Note on a method of determining the distribution of pore sizes in a porous material. PNAS 7:115–116. https://doi.org/10.1073/pnas.7.4.115

[49] Bratskaya S, Privar Y, Skatova A et al (2021) Carboxyalkylchitosan-based hydrogels with "imine clip": Enhanced stability and amino acids-induced disassembly under physiological conditions. Carbohydr Polym 274:118618. https://doi.org/10.1016/j.carbpol.2021.118618

[50] Li H, Chen Z, Zheng T et al (2021) A novel reaction-based fluorescent probe sensitive to pH changes in multiple intervals. Color Technol 137:154–165. https://doi.org/10.1111/cote.12515